nature energy

Article

https://doi.org/10.1038/s41560-023-01231-w

Critical interphase overpotential as a lithium dendrite-suppression criterion for all-solid-state lithium battery design

Received: 14 July 2022

Accepted: 17 February 2023

Published online: 16 March 2023

Check for updates

Hongli Wan[1,4], Zeyi Wang[1,4], Sufu Liu[1], Bao Zhang[2], Xinzi He[1], Weiran Zhang[3] & Chunsheng Wang[1]

Critical current density (CCD) is currently used to evaluate Li dendrite-suppression capability of solid-state electrolytes (SSEs). However, CCD values vary with engineering parameters, resulting in a large deviation of CCD values for the same SSE. Herein we evaluate lithium dendrite-suppression capability of SSEs using critical interphase overpotential (CIOP). The CIOP is the intrinsic property of the interphase, which depends on electronic/ionic conductivity, lithiophobicity and mechanical strength. When the applied interphase overpotential (AIOP) is larger than CIOP, Li will grow into interphase as dendrites. To reduce AIOP but increase CIOP, we design a mix-conductive Li_2NH-Mg interlayer between Li_6PS_5Cl SSE and Li-1.0 wt% La anode, which transfers into Li_6PS_5Cl/$LiMgS_x$/LiH-Li_3N/LiMgLa after Mg migration during annealing and activation cycles. The $LiMgS_x$ interphase increases the CIOP from ~10 mV (for Li_6PS_5Cl) to ~220 mV. The Li plates on the LiMgLa surface, and reversible penetration into formed porous LiH-Li_3N reduces AIOP. The CIOP provides a design guideline for high-energy and room temperature all-solid-state lithium-metal batteries.

All-solid-state lithium batteries (ASSLBs) can potentially achieve both high energy density and safety. However, the lithium dendrite growth and high interface resistance limit the cycle life of ASSLBs, especially at a high areal capacity, room temperature and low stack pressure. The solid–electrolyte interphase (SEI) from the reduction of solid-state electrolytes (SSEs) cannot block Li dendrite growth. Critical current density (CCD) is used to evaluate the lithium dendrite-suppression capability of SSE. CCD is defined as the current density that enables the Li dendrite to grow through the SEI and SSE and shorts the cell. CCD not only depends on the property of SEI but also depends on the SSE thickness, applied stack pressure and Li plating/stripping capacity/times and so on[1–5]. For example, the CCD value increases with the increase in SSE thickness but decreases with the increase of Li plating/stripping time/capacity. Therefore, the reported CCD values for the same SSE are widely scattered, making it very difficult to evaluate the lithium dendrite-suppression capability of the electrolytes.

Due to a lack of reliable Li dendrite-suppression criteria, the SSE design mainly relays on a trial-and-error strategy. Because Li dendrite is easy to grow through the void and grain boundary of a SSE, the SSE was densified or even synthesized as a single crystal, but Li dendrite still penetrated into the SSE[6–8]. Because the SEI formed on a SSE cannot suppress Li dendrite growth, artificial interphases (interlayers) with different electronic and ionic conductivity[9], lithiophobicity[10–13], Li solubility[14–16] and porosity[17,18] were inserted at the Li/SSE interface. The interlayer with high ionic conductivity and high lithiophobicity but very low electronic conductivity can prevent Li plating on the SSE surface, but it also increases the Li plating overpotential[12], while the lithiophilic alloy interlayer with a high electronic conductivity leads to Li deposition at the SSE surface, reducing the SSE.

Li dendrite starts to grow into interphase and SSE when the applied Li deposition overpotential on SEI (driving force) is

[1]Department of Chemical and Biomolecular Engineering, University of Maryland, College Park, MD, USA. [2]School of Physical and Mathematical Sciences, Nanyang Technological University, Singapore, Singapore. [3]Department of Materials Science and Engineering, University of Maryland, College Park, MD, USA. [4]These authors contributed equally: Hongli Wan, Zeyi Wang. e-mail: cswang@umd.edu

https://doi.org/10.1038/s41560-023-01231-w

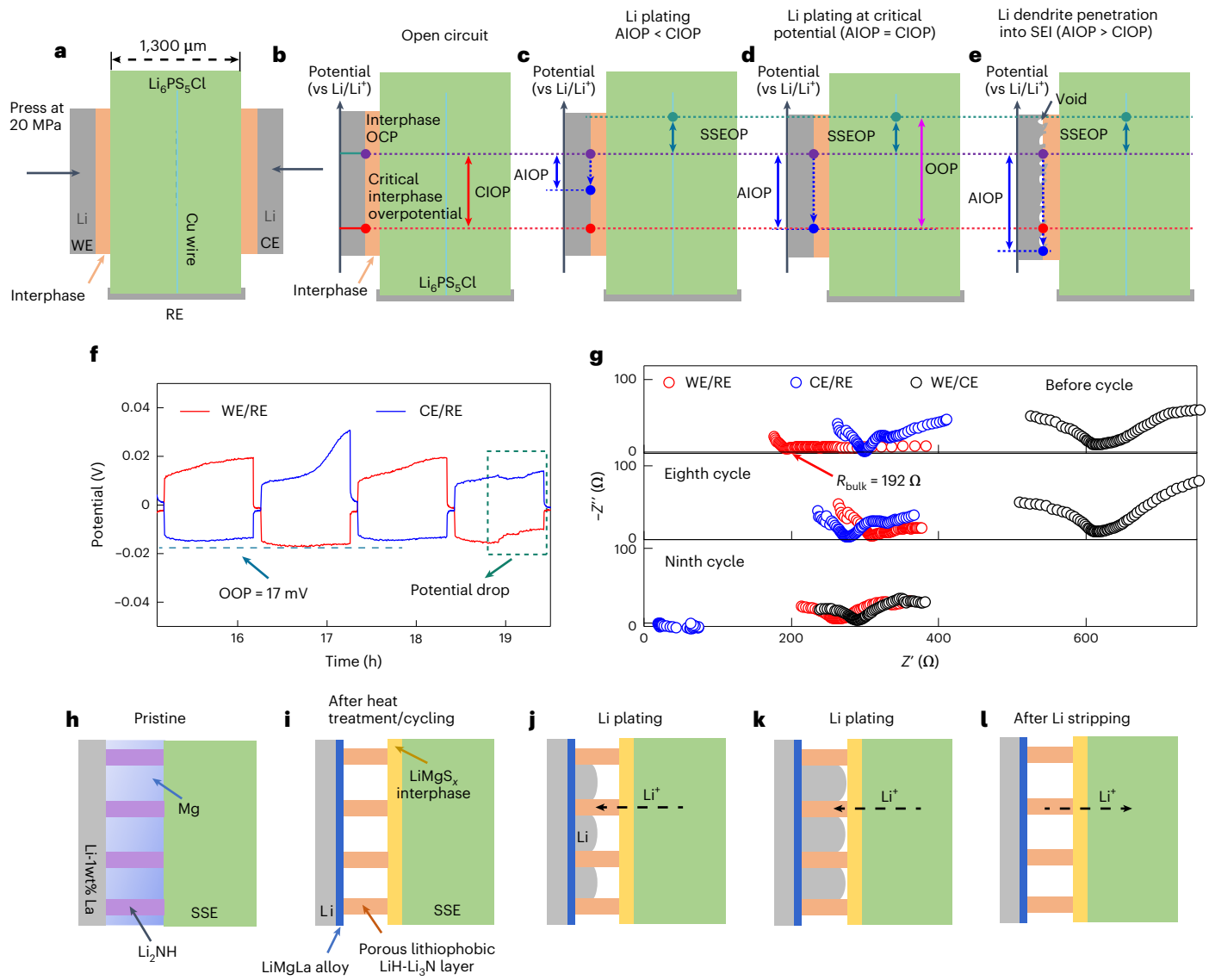

Fig. 1 | CIOP definition, designing principle and the realization of lithium dendrite-free interlayer. a, Configuration of three-electrode cell where one side of a copper wire is inserted inside of the Li_6PS_5Cl electrolyte pellet and the other side of the Cu wire is connected to the Li foil that is wrapped on a Li_6PS_5Cl electrolyte surface to serve as RE. **b**–**e**, Illustration of the correlation among OCP, OOP, SSEOP, AIOP and CIOP during Li plating. **f**, Potential profile of Li WE and Li CE during Li plating/stripping in the three-electrode cell shown in **a**. **g**, Impedance plots of Li working electrode (WE/RE), Li counter electrode (CE/RE) and the Li/Li_6PS_5Cl/Li full cell (WE/CE) before cycling, at the eighth cycle and at the ninth cycle. Charge/discharge current is 0.5 mA cm^{-2}, and the time for each charge and discharge is 1 h. **h**,**i**, The realization of an ideal interlayer by inserting the Li_2NH-Mg interlayer at the Li-1.0 wt% La/Li_6PS_5Cl interface, followed with annealing at 60 °C for 12 h to in situ form a $LiMgS_x$/porous and lithiophobic LiH-Li_3N/lithiophilic LiMgLa interlayer. **j**–**l**, Li plating/stripping process at the designed Li_6PS_5Cl/$LiMgS_x$/porous and lithiophobic LiH-Li_3N/lithiophilic LiMgLa interface.

larger than the critical interphase overpotential (resistance). The beginning of Li penetration into interphase (or SSE if it is stable with Li) is a critical step for Li dendrite shorting the cell, which depends only on the intrinsic property of the SEI (lithiophobicity, mechanical strength, ionic and electronic conductivity and so on), while the following Li dendrite growth through the entire SSE is controlled by the engineering parameters (SSE thickness, densification and so on). The engineering parameters (such as void at the Li/SEI interface, Li diffusivity, stack pressure) also affect the applied overpotential.

Instead of using CCD to evaluate the capability of the SSE to suppress Li dendrite growth through the entire SSE, herein we introduced a critical interphase overpotential (CIOP) to evaluate the capability of the interphase to suppress lithium dendrite breaking into the interphase at the Li/SSE interface. To achieve high lithium dendrite-suppression capability, the applied interphase overpotential (AIOP) should be low, and the CIOP of the SEI (or interphase) should be high. We used CIOP to evaluate the lithium dendrite-suppression capability of the SEI on Li_6PS_5Cl SSE and Li_2NH-Mg interlayer at Li/SSE interface. The Li_2NH-Mg interlayer enables the Li_6PS_5Cl electrolyte to achieve a high CIOP of 222.9 mV and CCD of 5.5 mA cm^{-2} / 5.5 mAh cm^{-2} at 25 °C and stable cycle up to 7.0 mA cm^{-2} / 7.0 mAh cm^{-2} at 60 °C. An all-solid-state lithium battery employing NMC622 cathode maintains a reversible capacity of 1.9 mAh cm^{-2} after 100 cycles at a current density of 0.76 mA cm^{-2} at 25 °C and a low stack pressure of 2.5 MPa.

Definition of CIOP

Sulfide solid electrolytes react with Li metal forming SEI, especially during Li plating at a negative potential (Fig. 1a and Supplementary Fig. 1a–d)[19–26]. The SEI growth will stop when the potential at SEI/SSE is above the reduction potential of SSE or the electronic conduction is blocked by SEI. At open-circuit potential (OCP), the SEI (or artificial interphase) potential at the SEI/Li interface is 0.0 V (vs Li^+/Li) (Fig. 1b

and Supplementary Fig. 2a). When an overpotential is applied to the Li anode (also on the SEI surface), Li begins to plate at the Li/SEI interface (Fig. 1c and Supplementary Fig. 2b). When the AIOP is equal to (Fig. 1d) or larger than (Fig. 1e) a CIOP[27], lithium dendrites begin to penetrate into (or form in) the SEI (Supplementary Fig. 2c). With further increasing the AIOP, the current density will increase, and Li dendrite further grows through interphase and penetrates into the SSE. When the current density is larger than a CCD, the Li dendrites grow through the entire SSE, resulting in a cell short circuit (Supplementary Fig. 2d). Therefore, CIOP presents the required overpotential for Li dendrite to begin penetration into the interphase, which depends on the intrinsic property of the interphase. CCD presents the required current for Li dendrite growth through the entire interphase and SSE and to short the cell, which not only depends on the property of interphase (CIOP) but also on the SSE thickness, applied pressure and Li plating/stripping capacity/times and so on. The CIOP is different from the critical overpotential (COP) defined by Yet-Ming Chiang et al.[6]. Their COP represents the capability of the SSE to suppress lithium grow in the SSE. If SEI is not formed on the SSE during Li plating, the CIOP of the interphase has a similar value as COP of the SSE. Because most SEI on SSEs have a low CIOP, artificial interphase is normally coated on SSEs to prevent the formation of unstable SEI. In this case, CIOP reflects the capability for the artificial interphase to suppress Li dendrite formation.

CIOP can be determined by subtraction of SSE overpotential (SSEOP) from the overall Li plating overpotential (OOP) when the Li dendrite forms (Fig. 1d). To accurately measure the Li plating overpotential, the position of Li reference electrode (RE) on the SSE was optimized. As shown in Supplementary Figs. 3 and 4, the Li dendrite growth and nucleation inside the Li_6PS_5Cl electrolyte cannot be monitored using the Li RE on both working electrode (WE) and counter electrode (CE) sides (Supplementary Note 1). To precisely monitor both cases, the lithium dendrite growth through SEI and Li dendrite formation inside the SSE, a Cu wire was inserted into Li_6PS_5Cl electrolyte, and another end is connected to the RE (Fig. 1a). Once lithium dendrites were formed at the interface of Li/interphase or inside the SSE, the potential of WE/RE and CE/RE will drop due to the increased electronic conduction at WE/RE and CE/RE. Once the lithium dendrite grows and reaches to Cu wire, the potential of WE/RE and CE/RE will drop to 0 V (vs Li^+/Li). The accuracy of the three-electrode cell with Cu–Li RE (Fig. 1a) was demonstrated by the identical value between the measured cell voltage (WE/CE: V1 in Supplementary Fig. 5) and calculated potential difference ($P_{WE/RE} - P_{CE/RE}$) (V2 in Supplementary Fig. 5). With a highly sensitive and reliable RE (RE_{Cu-Li}), the potentials of Li WE, Li CE and cell voltage during Li plating/stripping were monitored (Supplementary Figs. 5 and 6). The potential profile of WE and CE shows that the stripping potential (WE in Supplementary Fig. 6a and CE in Supplementary Fig. 6b) quickly increased with cycles due to the void accumulation in Li stripping/plating cycles, and then the cell was short circuited. The void accumulation increased the interface resistance as evidenced by the impedance at WE increase from 192 Ω (before cycle) to 308.6 Ω at the eighth cycle (Fig. 1g). At the ninth cycle (~19 h in Fig. 1f), the WE potential suddenly drops and CE is shorted with RE (Fig. 1g) due to lithium dendrite growth from CE into Li_6PS_5Cl and reach to RE. At this point, the lithium dendrite still did not propagate through the whole electrolyte layer, so the WE and CE were not connected by the lithium dendrite, as demonstrated by the normal non-short-circuit cell impedance of WE/CE at the ninth cycle (Fig. 1g). The optical cross-sectional visualization of Li/Li_6PS_5Cl interface also confirmed that the dark materials due to the reduction of Li_6PS_5Cl electrolytes and lithium dendrite did not connect WE to CE when the voltage drops (Supplementary Fig. 7a). The optical cross-sectional images of the short-circuit Li/Li_6PS_5Cl/Li cell also show that the WE and CE were fully connected by the dark materials (Supplementary Fig. 7b). Cross-section scanning electron microscope (SEM) images of the three-electrode cell were collected (before cycle, at the third cycle and after Li dendrite reaching to Cu–Li RE). As shown in Supplementary Fig. 8a, before cycling, no gap was observed at the Li/SEI interface. After three cycles, voids with small sizes were observed at the Li/SEI interface (marked by the red rectangle in Supplementary Fig. 8b). Upon further cycling, the formed voids will be accumulated into large sizes until the battery was short circuited (Supplementary Fig. 8c). The accumulation of voids at the Li/SEI interface also led to the AIOP surpassing CIOP, leading to the Li dendrites growing into SEI. Upon further Li plating/stripping cycles, Li dendrite penetrates through SEI and grows into Li_6PS_5Cl electrolyte. As shown in the backscattering electron images after CE potential drops (Supplementary Fig. 8d,e), the lithium dendrites (dark lines in Li_6PS_5Cl electrolyte in Supplementary Fig. 8d,e) connected the CE with RE_{Cu-Li} (red dashed line region in Supplementary Fig. 8e is the RE_{Cu-Li} position). The CE potential drop is because the AIOP surpasses the CIOP, leading to the Li dendrites penetrating into SEI. Upon further Li plating/stripping cycles, the voltage of the full cell dropped to ~0 V vs Li/Li^+ (Supplementary Fig. 5), and the cell was ultimately short circuited.

The unique Cu–Li RE in the three-electrode cell (Fig. 1a) enables us to accurately measure the CIOP, and the CIOP can be calculated by subtracting the bulk electrolyte overpotential from the electrode overpotential using the equation (1) and (2) (as demonstrated in Fig. 1b–e).

$$\mathrm{CIOP} = \mathrm{OOP} - \mathrm{SSEOP} \tag{1}$$

$$\mathrm{SSEOP} = A \times I \times R_{\mathrm{bulk}} \tag{2}$$

OOP (P_{WE} or P_{CE}) is the overall overpotential when the lithium dendrite is formed at WE or CE; that is, the electrode potential before potential drops due to Li dendrite (Fig. 1f, potential at WE/RE at eighth Li plating). SSEOP is the SSE overpotential (Fig. 1c–e), which is equal to $A \times I \times R_{bulk}$, where A (0.07065 cm^2) is the area of the Li WE or Li CE, I (0.5 mA cm^{-2}) is the applied current density and R_{bulk} (Fig. 1g) is the resistance of WE/RE or CE/RE that can be obtained by EIS. Because the voids are formed at the Li/SEI interface rather than the SEI/Li_6PS_5Cl interface (Fig. 1e, before Li penetration into SEI), the contact area of A is constant (0.07065 cm^2). Therefore, SSEOP is unchanged (Fig. 1c–e) before Li penetrates through the interphase.

We measured the CIOPs of SEI in Li_6PS_5Cl SSE with different electrolyte thicknesses and different electrolyte densification under different pressures. For comparison, we also measured the CIOPs of the SEI in different electrolytes (Li_6PS_5Cl, $Li_6PS_5Cl_{0.7}F_{0.3}$, and Li_6PS_5Cl-CuF_2-$LiNO_3$ (Li_6PS_5Cl-CL (ref. [28])). By using the OOP values; R_{bulk} values, A values and equations (1)and (2), the CIOPs of the SEI in Li_6PS_5Cl, $Li_6PS_5Cl_{0.7}F_{0.3}$ and Li_6PS_5Cl-CL electrolytes with different electrolyte thickness, densification and testing pressure were calculated and shown in Table 1.

The CIOP of SEI in Li_6PS_5Cl electrolytes with different thicknesses, densification and testing pressure is similar (9 mV to approximately 12 mV). When the pressure decreases from 20 MPa (Fig. 1a) to 10 MPa (Supplementary Fig. 9), the CIOP of the SEI in 1.3 mm Li_6PS_5Cl electrolyte only slightly increases from 10 mV to 11 mV (Fig. 1a vs Supplementary Fig. 9). When the thickness of the electrolyte decreases from 1.3 mm to 1.0 mm, the CIOP of the SEI in Li_6PS_5Cl electrolyte slightly increased from 11 mV to 12 mV (Supplementary Figs. 9 vs 10). When the densification of the Li_6PS_5Cl electrolyte decreases (Supplementary Figs. 11 and 14), the CIOP of the Li_6PS_5Cl electrolyte slightly decreases from 12 mV to 9 mV (Supplementary Figs. 10 vs 11). The variation of 3 mV for the SEI in the Li_6PS_5Cl electrolyte is within the sensitivity of the measurement. When Cl in the Li_6PS_5Cl electrolyte is partially replaced by F (Supplementary Figs. 12 and 15), the CIOP largely increases from ~12 mV to 49 mV (Supplementary Figs. 10 vs 12). This is because LiF has a much higher interface energy against Li than that of LiCl (ref. [13]). In addition, the

Table 1 | CIOPs for different SEI

SSE	Li_6PS_5Cl[a]	Li_6PS_5Cl[b]	Li_6PS_5Cl[c]	Li_6PS_5Cl[d]	$Li_6PS_5Cl_{0.7}F_{0.3}$[e]	Li_6PS_5Cl-CL[f]
SSE densification	high	high	high	low	high	high
Pressure (MPa)	20	10	10	10	10	10
Thickness (μm)	1,300	1,300	1,000	1,000	1,000	1,000
SEI	Li_2S-Li_3P-LiCl	Li_2S-Li_3P-LiCl	Li_2S-Li_3P-LiCl	Li_2S-Li_3P-LiCl	Li_2S-Li_3P-LiCl-LiF	Li_2S-Li_3P-LiCl-LiF-Li_3N
OOP (mV)	17.0	23.8	22.6	19.3	66.7	81.6
R (Ω)	192	361	296.5	296.9	498	109
CIOP (mV)	10.2	11	12.1	9	49.1	77.7
CCD (mA cm^{-2}/mAh cm^{-2}@1MPa)	-	0.6	0.4	-	0.6	1.4

CIOP for SEI in Li_6PS_5Cl (Fig. 1a and Supplementary Figs. 9–11), $Li_6PS_5Cl_{0.7}F_{0.3}$ (Supplementary Fig. 12) and Li_6PS_5Cl-CuF_2-$LiNO_3$ (Li_6PS_5Cl-CL; Supplementary Fig. 13) electrolytes with different electrolyte thickness, densification and testing pressure at room temperature. [a]The details were shown in Fig. 1a–g. [b]The details were shown in Supplementary Fig. 9. [c]The details were shown in Supplementary Fig. 10. [d]The details were shown in Supplementary Fig. 11. [e]The details were shown in Supplementary Fig. 12. [f]The details were shown in Supplementary Fig. 13.

electronic conductivity of the obtained $Li_6PS_5Cl_{0.7}F_{0.3}$ electrolyte (1.6×10^{-8} S cm^{-1}; Supplementary Fig. 16) is lower than that of Li_6PS_5Cl electrolyte (7.1×10^{-8} S cm^{-1}), which also suppressed the Li plating inside $Li_6PS_5Cl_{0.7}F_{0.3}$ electrolyte. Further introducing highly ionic-conductive Li_3N into LiF-rich SEI (the SEI formed from the reduction of Li_6PS_5Cl-CL (ref. [28])), the CIOP of Li_3N-LiF-rich SEI increases to 77.7 mV (Supplementary Fig. 13). At the fixed SSE thickness and pressure, the increase of CIOP of SEI also enhances the CCD of the SSE. CCD of 1,000 μm Li_6PS_5Cl is 0.4 mA cm^{-2}/ 0.4 mAh cm^{-2} (Supplementary Fig. 17). After doping F, the CCD of 1,000 μm $Li_6PS_5Cl_{0.7}F_{0.3}$ electrolyte increased to 0.6 mA cm^{-2}/ 0.6 mAh cm^{-2} (Supplementary Fig. 18). After F and N co-doping, the CCD of 1,000 μm Li_6PS_5Cl-CuF_2-$LiNO_3$ electrolyte[28] reaches to 1.4 mA cm^{-2}/ 1.4 mAh cm^{-2}. In summary, CIOP is the overpotential that Li dendrites begin to penetrate into (or form in) the interphase, which is an intrinsic property of SEI and is independent of electrolyte thickness, testing pressure and densification (Table 1). CCD is the current that Li dendrite has grown through SSE and shorted the cell, which is an engineering parameter of the SSE.

To achieve high-energy and long-cycle-life ASSLB at room temperature and a low stack pressure, the interlayer between Li and SSE should have the AIOP/CIOP ratio of <1 (that is, dendrite free). The SSE reduction, voids formation and high interphase resistance (Supplementary Fig. 1) will increase AIOP[5,24,25,29], while the enhanced lithiophobicity of the interphase can increase the CIOP. In detail, the interlayer at the Li/SSE interface should be porous and lithiophobic with high ionic conductivity and moderate electronic conductivity to enable highly reversible Li penetration/extraction into/from pores during Li plating/stripping cycles (Fig. 1i–l). In addition, a robust SEI should be formed on the SSE surface to prevent SSE from reduction even if Li was fully filled into the pores at a high Li-plating capacity (Fig. 1k). To avoid the formation of voids at the Li/porous interlayer during overstripping of Li, a lithiophilic Li–M alloy layer that can strongly bond the skeleton of the interlayer to Li anode is highly desired[16] (Fig. 1i–l). The lithiophobic/self-passivated SEI on the SSE surface can ensure a high CIOP, while porous interlayer and lithiophilic Li–M alloy with high Li diffusivity[10,14,30,31] can reduce AIOP. However, such an ideal interlayer between Li and SSE is very challenging to be fabricated and has not been reported yet.

Due to the small CIOP (9 mV to approximately 12 mV) of SEI (not artificial SEI) on Li_6PS_5Cl electrolyte surface, artificial interphase with a high CIOP is required to suppress lithium dendrite. Under the guidance of the artificial SEI design principle (AIOP/CIOP ratio of <1), we designed such intelligent artificial SEI by inserting Li_2NH-Mg composite interlayer between Li-1.0 wt% La anode (the weight ratio of La in Li was 1.0 wt%) and Li_6PS_5Cl SSE, and followed with heat treatment at 60 °C for 12 h (Fig. 1h,i). We used Li-1.0 wt% La rather than Li to increase the Li diffusivity suppressing void formation between Li-1.0 wt% La and artificial interphase. During heat treatment, Li_2NH is decomposed into LiH-Li_3N, and Mg in the interlayer reacted with Li_6PS_5Cl SSE in situ forming a passivating $LiMgS_x$ layer between LiH-Li_3N interlayer and Li_6PS_5Cl (Fig. 1i). Other Mg in Li_2NH-Mg interlayer is lithiated and migrated to the bottom Li-1.0 wt% La anode forming lithiophilic LiMgLa alloy that is strongly bonded to LiH-Li_3N (Fig. 1h,i). After Mg reaction and migration, Li_6PS_5Cl/Li_2NH-Mg/Li-1wt% La transfers into Li_6PS_5Cl/$LiMgS_x$/LiH-Li_3N/LiMgLa, where self-passivated $LiMgS_x$ can increase the CIOP, while Li plating at LiMgLa surface and reversible penetration/extraction into/from the porous lithiophobic and ionic-conductive LiH-Li_3N (Fig. 1j–l) can reduce AIOP.

Demonstrating the formation of LiMgLa/LiH-Li_3N/$LiMgS_x$/Li_6PS_5Cl

Li_2NH-Mg composite was prepared by ball milling of Li_2NH and Mg at a weight ratio of 1:1 (Supplementary Figs. 19–21; the particle size of Li_2NH-Mg was 0.5 μm to approximately 4 μm; detailed preparation procedures can be found in the Methods and Supplementary Information). To monitor the Mg migration from Li_2NH-Mg to Li anode, a Li_2NH-Mg/Li bi-layer was prepared by rolling the Li_2NH-Mg powder on the surface of Li metal. After heat treatment of Li_2NH-Mg/Li at 60 °C for 12 h, Li_2NH-Mg/Li transformed into LiH-Li_3N/LiMg. As shown in X-ray powder diffraction (XRD) pattern (Supplementary Fig. 22), the diffraction peaks for Li_2NH and Mg disappeared, but Li–Mg alloy peak appeared after heat treatment. The time-of-flight secondary ion mass spectroscope (ToF-SIMS) spectra was also collected on the surface of Li_2NH-Mg/Li before and after heat treatment. ToF-SIMS characterization in Fig. 2 shows that H^+ (an indicator of Li_2NH) was presented in the Li_2NH-Mg layer before heat treatment (Fig. 2a). However, after heat treatment, the H^+ signal disappeared (Fig. 2b), while the H^- intensity (an indicator of LiH) appears and maintains constant in Li_2NH-Mg (Fig. 2b), demonstrating the transformation of Li_2NH to LiH-Li_3N after heat treatment. LiH is highly lithiophobic as demonstrated by a high contact angle of 135.6° (Supplementary Fig. 23). The LiH can effectively suppress Li dendrite, as demonstrated by the increased CCD from 0.4 mA cm^{-2}/ 0.4 mAh cm^{-2} for pristine Li_6PS_5Cl (Supplementary Fig. 17) to 1.1 mA cm^{-2}/ 1.1 mAh cm^{-2} for LiH-coated Li_6PS_5Cl (Supplementary Fig. 24) at room temperature.

A Cu/Li_6PS_5Cl/Li_2NH-Mg/Li triple layer was assembled to investigate the reaction of Mg (in Li_2NH-Mg) with Li_6PS_5Cl electrolyte during heat treatment. After heat treatment and charge/discharge cycling, the Cu/Li_6PS_5Cl layer was removed, and the exposed Li_2NH-Mg surface was characterized using SEM, energy dispersive spectroscopy (EDS) and ToF-SIMS. The formation of $LiMgS_x$ on the LiH-Li_3N surface is proved by the Mg^+ enrichment on the LiH-Li_3N surface (Fig. 2d). The intensity of Mg^+ inside LiH-Li_3N drop from 4×10^{-4} a.u. in fresh Li_2NH-Mg (Fig. 2c) to 1×10^{-4} a.u. after heat treatment and cycling (Fig. 2d) confirmed the Mg migration to Li anodes during heat treatment and cycling, which is in agreement with the XRD results in Supplementary Fig. 22. The Mg migration into the Li layer after Li plating/stripping cycles can also be observed in Fig. 2e, while elemental N still maintains at the LiH-Li_3N/Li

https://doi.org/10.1038/s41560-023-01231-w

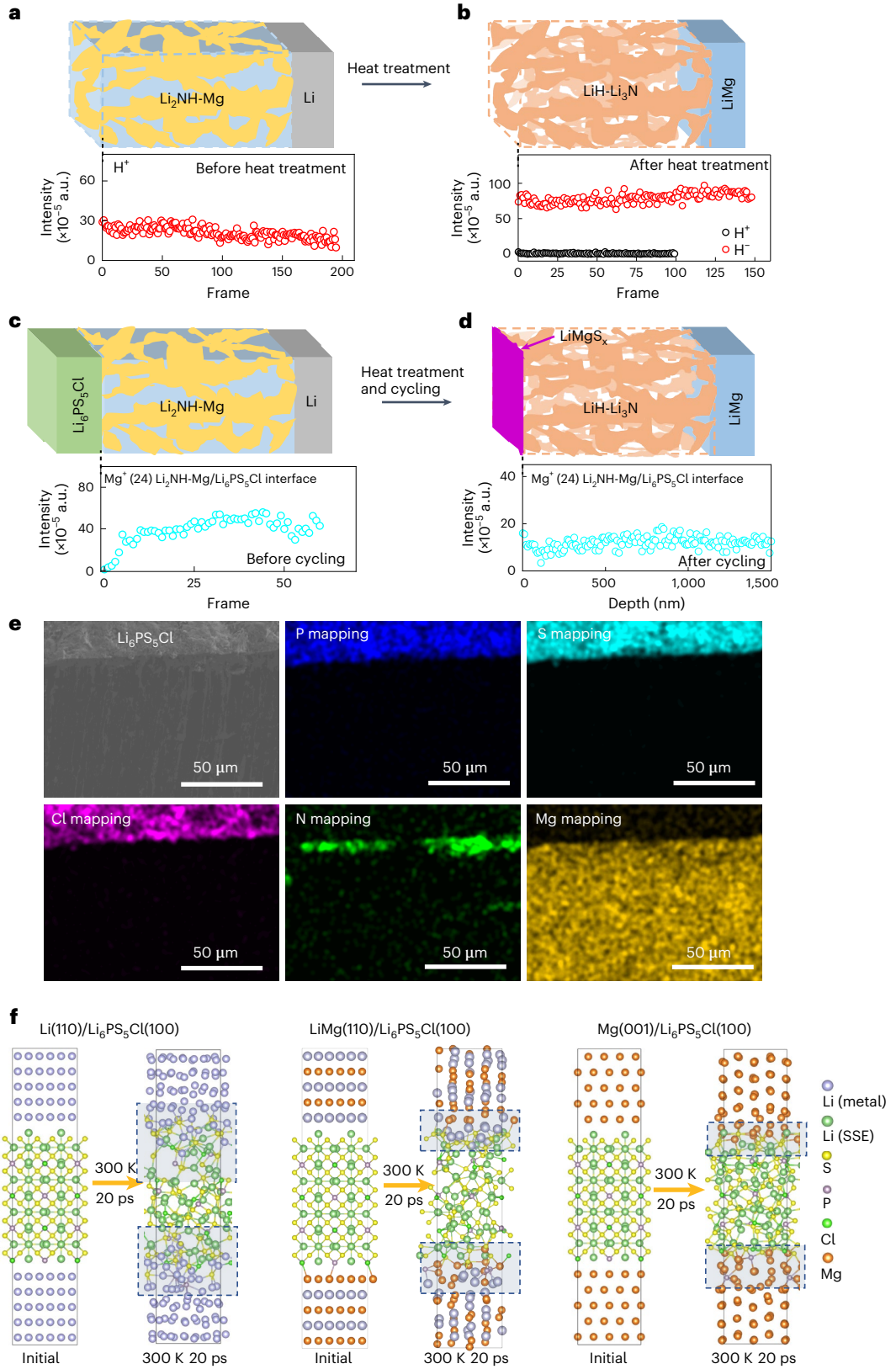

Fig. 2 | Ion and element distribution, morphology of interlayer with Li anode and Li_6PS_5Cl electrolyte. a, H^+ distribution before heat treatment. **b**, H^+ and H^- distribution after heat treatment. **c**,**d**, Mg^+ distribution at the Li_2NH-Mg/Li_6PS_5Cl interface before (**c**) and after (**d**) heat treatment and 50 Li plating/stripping cycles. **e**, SEM and EDS images of the Li_6PS_5Cl/$LiMgS_x$/LiH-Li_3N/LiMg interface after 50 cycles. **f**, Illustration of structural change of Li/Li_6PS_5Cl, LiMg/Li_6PS_5Cl and Mg/Li_6PS_5Cl predicated by AIMD simulations.

https://doi.org/10.1038/s41560-023-01231-w

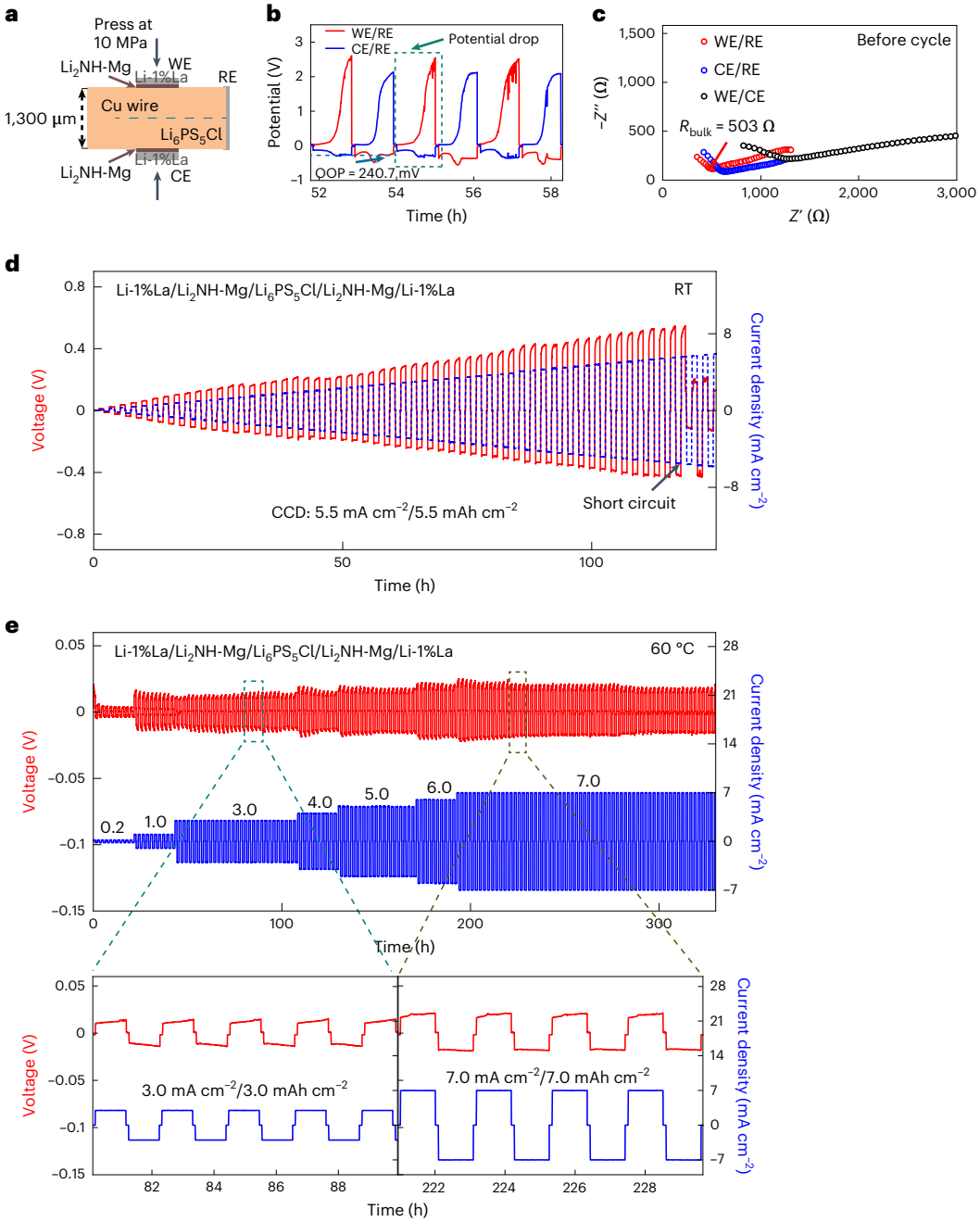

Fig. 3 | CIOP and CCD of Li_6PS_5Cl electrolyte with Li_2NH-Mg interlayer inserted between Li-1.0 wt% La and Li_6PS_5Cl. **a**, Cell configuration of Li-1.0 wt% La/Li_6PS_5Cl/Li-1.0 wt% La three-electrode cell with Li_2NH-Mg interlayer. **b**, Potential profile of Li WE and Li CE of Li-1.0 wt% La/Li_6PS_5Cl/Li-1.0 wt% La three-electrode cell with Li_2NH-Mg interlayer. **c**, Impedance of WE, CE and full cell before cycle in Li-1.0 wt% La/Li_2NH-Mg/Li_6PS_5Cl/Li_2NH-Mg/Li-1.0 wt% La three-electrode cell. **d**,**e**, Voltage profile of Li-1.0 wt% La/Li_2NH-Mg/Li_6PS_5Cl/Li_2NH-Mg/Li-1.0 wt% La two-electrode cell tested at step-increase current density/capacity under room temperature (**d**) and temperature of 60 °C (**e**).

interface. The $LiMgS_x$ interphase can passivate Li_6PS_5Cl electrolytes and suppress the lithium dendrite growth as evidenced by the absence of dark area in the backscattering images of Li_6PS_5Cl that is contacted with Li_2NH-Mg@Li anode (Supplementary Fig. 25; before characterization, the Li_2NH-Mg@Li anode was removed from the Li_6PS_5Cl/Li_2NH-Mg@Li pellet). The ab initio molecular dynamic (AIMD) simulation results also confirmed (Fig. 2f and Supplementary Fig. 26) that when Li–Mg contact with Li_6PS_5Cl, the thin Li–Mg–S-containing layer was formed on the both Li–S end side and the Li–P–Cl end side, inhibiting the side reaction between LiMg and Li_6PS_5Cl. When pure Mg in Li_2NH-Mg interlayer came in contact with Li_6PS_5Cl, the interface between Mg and Li_6PS_5Cl was further stabilized, implying the in situ formed passivated Li–Mg–S thin layer in both Li-rich LiMg and Li-poor LiMg can reduce the decomposition of Li_6PS_5Cl electrolyte and allows the electrolyte to be stabilized during the cycles. In sharp contrast, Li atoms at the Li/Li_6PS_5Cl interface can migrate into Li_6PS_5Cl, forming highly disordered Li–P–S–Cl bond networks (Fig. 2f) because the Li/Li_6PS_5Cl interface is unstable and the Li/Li_6PS_5Cl interphase cannot block the reduction reaction and Li dendrite growth.

The intimate contact between the deposited Li and LiH-Li_3N through the bonding effect of the lithiophilic Li–Mg alloy was also confirmed by SEM. The SEM images were collected at Li/LiH-Li_3N

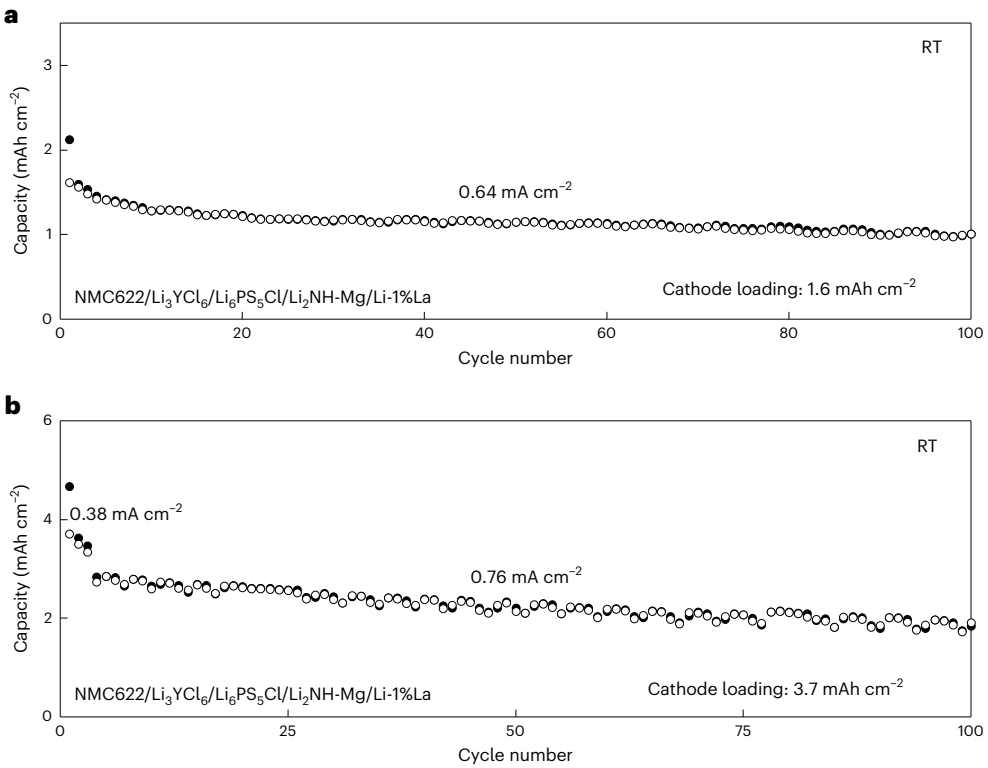

Fig. 4 | Electrochemical performance of NMC622/Li_3YCl_6/Li_6PS_5Cl/Li_2NH-Mg/Li-1.0 wt% La cell. a,**b**, Electrochemical performance of NMC622/Li_3YCl_6/Li_6PS_5Cl/Li_2NH-Mg/Li-1.0 wt% La cell at room temperature under cathode loading of 1.6 mAh cm^{-2} (**a**) and 3.7 mAh cm^{-2} (**b**).

interface (the craters for the SEM characterization were obtained by Ga^+ sputtering). Before characterization, Li_6PS_5Cl was removed from the Li_6PS_5Cl/Li_2NH-Mg/Li pellet after several Li plating/stripping cycles, and the SEM images of Li/Li_2NH-Mg (from top to bottom) were collected. As shown in Supplementary Fig. 27, no obvious voids were observed at the Li/LiH-Li_3N interface after Li plating/stripping cycles. All the characterization confirmed the in situ formation of LiMgLa/LiH-Li_3N/$LiMgS_x$/Li_6PS_5Cl from Li-1.0 wt% La/Li_2NH-Mg/Li_6PS_5Cl after Li plating/stripping cycles.

Cell performance using a Li_2NH-Mg interlayer

Similar to LiF, LiH in LiH-Li_3N is also lithiophobic. In addition, LiH has much higher ionic conductivity (2.7×10^{-8} mS cm^{-1}; Supplementary Fig. 28) than LiF. The higher ionic conductivity of LiH can decrease the Li plating/stripping overpotential, as demonstrated by the lower overpotential of Li/Li_6PS_5Cl/Li cell using LiH-Mg interlayer than that using LiF-Mg interlayer (Supplementary Fig. 29). Introduction of Li_3N in LiH by in situ decomposition of Li_2NH can further increase the ionic conductivity of the lithiophobic interphase from 2.7×10^{-8} mS cm^{-1} to 7.9×10^{-5} S cm^{-1} (Supplementary Fig. 28d), which can further reduce the Li plating/stripping overpotential. In addition, LiH-Li_3N also has a larger lithiophobicity (contact angle: 143.7°; Supplementary Fig. 30) than that of LiH (contact angle: 135.6°; Supplementary Fig. 23). The Li_2NH-Mg interlayer enabled formation of $LiMgS_x$ interphase achieving a high CIOP of 222.9 mV (Fig. 3a–c), which is 20 times higher than that of bare Li_6PS_5Cl electrolyte (9 mV to approximately 12 mV). When Li-1.0 wt% La anode was replaced by Li anode, the CIOP maintains a similar value (219.6 mV; Supplementary Fig. 31), further proving that the CIOP is the intrinsic property of the interphase and is not affected by the Li anodes. The high CIOP also enhanced the CCD to 5.5 mA cm^{-2}/ 5.5 mAh cm^{-2} (Fig. 3d), which is much higher than that of bare Li_6PS_5Cl electrolyte (0.4 mA cm^{-2}/ 0.4 mAh cm^{-2}, Supplementary Fig. 17a)[28]. When increasing the testing temperature to 60 °C, the Li-1.0 wt% La/Li_6PS_5Cl/Li-1.0 wt% La cells with Li_2NH-Mg interlayer can even stably charge/discharge at 7.0 mA cm^{-2}/ 7.0 mAh cm^{-2} (Fig. 3e). The introduction of La in Li–Mg alloy can improve the lithium diffusion in Li metal due to refined grain size, resulting in reduced overpotential of cells using Li-1.0 wt% La anodes (Fig. 3d) than that using Li anode (Supplementary Fig. 32) during step-increase current density/capacity tests at room temperature.

In summary, the Li_6PS_5Cl/$LiMgS_x$/LiH-Li_3N/LiMgLa is in situ formed from Li_6PS_5Cl/Li_2NH-Mg/Li-1.0 wt% La after heat treatment and initial charge/discharge activation cycles. $LiMgS_x$ with a high CIOP of ~220 mV suppressed Li dendrite growth, while the porous LiH-Li_3N and high Li diffusive LiMgLa anode reduced AIOP because the Li penetration into porous LiH-Li_3N will increase the contact area between deposited Li and LiH-Li_3N, and the LiMgLa layer strongly welds the Li-1.0 wt% La anode to the LiH-Li_3N interlayer, maintaining intimate contact. CIOP of the SEI is an intrinsic property of the SEI, so the CIOP value (~10 mV) of SEI in Li_6PS_5Cl (Supplementary Figs. 10 and 33) and the CIOP (~220 mV) of the Li_2NH-Mg interphase (Fig. 3a–c, Supplementary Fig. 31) are independent of Li or Li-1.0 wt% La anodes (Supplementary Table 1). CCD is an engineering parameter, which is affected by both CIOP and Li anode (Supplementary Fig. 34 and Supplementary Table 1). Because both the Li penetration into and nucleation inside the interphase drop the overpotential, the CIOP of the interphase represents the suppressing capability for both Li nucleation in the interphase and Li growth into the interphase. In addition, the interphase potential is much lower than SSE potential during Li plating (Supplementary Fig. 35a), and the Li nucleation in interphase is much easier than in SSE. The interphase with higher CIOP can prevent the Li nucleation in the SSE (Supplementary Fig. 35a), while Li can nucleate in the SSE (red region in Supplementary Fig. 35b) if interphase does not exist.

The electrochemical performance of ASSLB employing the Li_2NH-Mg interlayer, Li-1.0 wt% La anode and NMC622 cathodes was evaluated at room temperature. As shown in Fig. 4b, NMC622/Li_3YCl_6/Li_6PS_5Cl/Li_2NH-Mg/Li-1.0 wt% La battery provided a high reversible

capacity of 2.7 mAh cm^{-2} at a current density of 0.76 mA cm^{-2} and maintains at 1.9 mAh cm^{-2} after 100 cycles. When decreasing the cathode loading, the battery delivers a capacity of 1.0 mAh cm^{-2} at 0.64 mA cm^{-2} after 100 cycles (Fig. 4a). Further decreasing the areal capacity to 1.3 mAh cm^{-2}, the $LiNiO_2/Li_3YCl_6/Li_6PS_5Cl/Li_2NH$-Mg/Li-1.0 wt% La cell can also stable cycle at 0.1 C for >250 cycles (Supplementary Fig. 36). To evaluate the battery performance at higher cathode loading, the testing temperature was increased to 60 °C to improve the Li^+ conduction in the ultra-thick cathode layer. As shown in Supplementary Fig. 37, at cathode loading of 13.8 mAh cm^{-2}, a high reversible capacity of 12.2 mAh cm^{-2} was maintained after ten cycles for NMC622/Li_3YCl_6/Li_6PS_5Cl/Li_2NH-Mg/Li-1.0 wt% La battery at a current density of 1.0 mA cm^{-2}. When the Li-1.0 wt% La anode was replaced by Li anode, the NMC622/$Li_3YCl_6/Li_6PS_5Cl/Li_2NH$-Mg/Li cell with an areal capacity of 2.6 mAh cm^{-2} can also stable cycle for 100 cycles at a current density of 0.5 mA cm^{-2} and room temperature (Supplementary Fig. 38). In sharp contrast, the cell without the Li_2NH-Mg interphase was short circuited in the sixth cycle at a low areal capacity of 1.67 mAh cm^{-2} (Supplementary Fig. 39), further proving the high Li dendrite-suppression capability of the Li_2NH-Mg interphase with high CIOP.

Conclusions

From Li dendrite-growth mechanism, the Li dendrite-suppression capability can be accurately evaluated by CIOP, an intrinsic property of the SEI on solid electrolytes, representing that once the AIOP is larger than CIOP, Li will break through SEI and develop into dendrite. CCD is the maximum current density for Li dendrites growing through the SSE and shorting the cell. CCD not only depends on the intrinsic electrolyte property (CIOP) but is also affected by SSE thickness, testing pressure, densification of SSE and the Li anode (AIOP). We measured the CIOPs of Li_6PS_5Cl (9 mV to approximately 12 mV), $Li_6PS_5Cl_{0.7}F_{0.3}$ (49 mV), Li_6PS_5Cl-CuF_2-$LiNO_3$ (77.7 mV) and the designed Li_2NH-Mg interlayer using three-electrode cells. The Li_2NH-Mg interlayer enables the Li_6PS_5Cl electrolyte to achieve a CIOP of ~220 mV and high CCD of 5.5 mA cm^{-2}/5.5 mAh cm^{-2} at room temperature. NMC622/$Li_3YCl_6/Li_6PS_5Cl/Li_2NH$-Mg/Li-1.0 wt% La battery delivers a high reversible capacity of 1.9 mAh cm^{-2} after 100 cycles at a current density of 0.76 mA cm^{-2} and room temperature.

Methods

Preparation of Li_2NH, Li_2NH-Mg, LiH-Mg, LiF-Mg, Li-1.0 wt% La alloy and Li_2NH-Mg/Li-1.0 wt% La anode

The lithium imide (Li_2NH) was prepared from dehydrogenation reaction of lithium amide ($LiNH_2$, 95%, Sigma–Aldrich) and lithium hydride (LiH, 95%, Sigma–Aldrich). First, the mixture of $LiNH_2$ and LiH with molar ratio of 1:1 were ball milled (PM 100, Retsch) at 500 r.p.m. for 12 h in an argon-filled atmosphere. Then, the mixture was subjected to a programmed thermal desorption at 300 °C for 24 h with heating rate of 5 °C min^{-1} in a homemade stainless-steel tube. After that, the light-green Li_2NH powder was obtained after cooling at a rate of 5 °C min^{-1}.

Li_2NH-Mg was prepared by ball milling Li_2NH and Mg powder with weight ratio of 1:1 at 400 r.p.m. for 1.0 h under an argon-filled atmosphere. LiH-Mg and LiF-Mg were prepared by the same procedures as Li_2NH-Mg by replacing Li_2NH to LiH and LiF, respectively.

La-doped Li anode (Li-1.0 wt% La) was prepared by melting Li and La at 400 °C; the weight ratio of La in Li was 1%.

Li_2NH-Mg/Li-1.0 wt% La anode was prepared by rolling the Li_2NH-Mg powder on the surface of Li-1.0 wt% La alloy.

Materials characterization

X-ray powder diffraction (XRD) was performed on D8 Advance with LynxEye and SolX (Bruker) using Cu *K*α radiation. The morphologies and element distribution were obtained on a field-emission scanning electron microscope (SEM, SU-70, Hitachi) equipped with an energy dispersive spectroscopy (EDS). The distribution of different elements was analysed on Ga^+ focused ion beam/scanning electron microscope (Tescan GAIA3) equipped with time-of-flight secondary ion mass spectroscope (ToF-SIMS).

Electrochemical measurements

The two-electrode symmetric cell was assembled as follows. First, Li_6PS_5Cl electrolyte powder was pressed at 6 tons to form a pellet with diameter of 10 mm. After that, lithium foil with diameter of 10 mm was attached on both sides of the electrolyte pellet. The formed Li/Li_6PS_5Cl/Li cell was then sandwiched between two stainless-steel rods. In the case of the three-electrode cell, lithium foils with diameters of 3 mm were first concentrically attached on both sides of the Li_6PS_5Cl electrolyte pellet (diameter: 10 mm) as working electrode and counter electrode. Then, a lithium reference electrode with a diameter of 0.5 mm was placed beside the working electrode or counter electrode. To explore lithium dendrite formation, Cu wire was incorporated in the centre of the Li_6PS_5Cl electrolyte pellet. Then, the Cu wire was wrapped by lithium and served as the lithium reference electrode. All the assembled three-electrode cells were sealed in coin cells, and the cell configuration is shown in Fig. 1 and Supplementary Figs. 3, 4.

The two-electrode all-solid-state full cell was assembled as following. First, NMC622, Li_3YCl_6 electrolyte and carbon nanotube (CNT) with weight ratio of 60:40:3 was hand mixed to form a composite cathode. Then, 60 mg of Li_6PS_5Cl and 60 mg of Li_3YCl_6 electrolyte was pressed at 4 tons to form an electrolyte bi-layer. After that, the composite cathode material was spread on the side of Li_3YCl_6 electrolyte and pressed at 6 tons. Finally, Li_2NH-Mg/Li-1.0 wt% La anode was attached on the side of the Li_6PS_5Cl electrolyte layer. An all-solid-state battery employing $LiNiO_2$ composite cathode ($LiNiO_2$ composite cathode was prepared by hand mixing NMC622 and Li_3YCl_6 with weight ratio of 70:30) was assembled by the same procedures mentioned above.

Galvanostatic cycling of both two-electrode and three-electrode cells were conducted on Arbin BT2000 workstation (Arbin Instruments) at room temperature. The cycling performance of the three-electrode cell was performed at a constant current density of 0.5 mA cm^{-2}; the time for the lithium stripping or plating process was 1.0 hour. The three-electrode cells were rested for 6 h to stabilize the interface between Li reference and Li_6PS_5Cl electrolyte before testing.

Computational methods

The AIMD simulations[32,33] were performed by using Vienna Ab-initio Simulation Package[34] with Projector Augmented Wave method[35]. And the exchange–correlation energy is described by the functional of Perderw, Burke and Ernzerhof form[36,37]. The NVT simulations are carried at 300 K with a time step of 1 fs. A Gamma-point only calculation with an energy cut-off of 400 eV was used. All of the atomic structures are visualized by VESTA[38].

Data availability

The data supporting the findings of this study are available within the article and its Supplementary Information files.

References

1. Ren, Y., Shen, Y., Lin, Y. & Nan, C.-W. Direct observation of lithium dendrites inside garnet-type lithium-ion solid electrolyte. *Electrochem. Commun.* **57**, 27–30 (2015).
2. Bay, M. C. et al. Sodium plating from Na-β″-alumina ceramics at room temperature, paving the way for fast-charging all-solid-state batteries. *Adv. Energy Mater.* **10**, 1902899 (2019).
3. Han, F., Yue, J., Zhu, X. & Wang, C. Suppressing Li dendrite formation in Li_2S-P_2S_5 solid electrolyte by LiI incorporation. *Adv. Energy Mater.* **8**, 1703644 (2018).
4. Suyama, M., Kato, A., Sakuda, A., Hayashi, A. & Tatsumisago, M. Lithium dissolution/deposition behavior with Li_3PS_4-LiI electrolyte for all-solid-state batteries operating at high temperatures. *Electrochim. Acta* **286**, 158–162 (2018).

5. Dixit, M. B. et al. In situ investigation of chemomechanical effects in thiophosphate solid electrolytes. *Matter* **3**, 2138–2159 (2020).
6. Porz, L. et al. Mechanism of lithium metal penetration through inorganic solid electrolytes. *Adv. Energy Mater.* **7**, 1701003 (2017).
7. Cheng, E. J., Sharafi, A. & Sakamoto, J. Intergranular Li metal propagation through polycrystalline $Li_{6.25}Al_{0.25}La_3Zr_2O_{12}$ ceramic electrolyte. *Electrochim. Acta* **223**, 85–91 (2017).
8. Liu, G. et al. Densified Li_6PS_5Cl nanorods with high ionic conductivity and improved critical current density for all-solid-state lithium batteries. *Nano Lett.* **20**, 6660–6665 (2020).
9. Kim, S. Y. & Li, J. Porous mixed ionic electronic conductor interlayers for solid-state batteries. *Energy Mater. Adv.* **2021**, 1519569 (2021).
10. Choi, H. J. et al. In situ formed Ag-Li intermetallic layer for stable cycling of all-solid-state lithium batteries. *Adv. Sci.* **9**, e2103826 (2021).
11. Cui, C. et al. Unlocking the in situ Li plating dynamics and evolution mediated by diverse metallic substrates in all-solid-state batteries. *Sci. Adv.* **8**, eadd2000 (2022).
12. Ji, X. et al. Solid-state electrolyte design for lithium dendrite suppression. *Adv. Mater.* **32**, 2002741 (2020).
13. Fan, X. et al. Fluorinated solid electrolyte interphase enables highly reversible solid-state Li metal battery. *Sci. Adv.* **4**, eaau9245 (2018).
14. Lee, Y.-G. et al. High-energy long-cycling all-solid-state lithium metal batteries enabled by silver-carbon composite anodes. *Nat. Energy* **5**, 299–308 (2020).
15. Raj, V. et al. Direct correlation between void formation and lithium dendrite growth in solid-state electrolytes with interlayers. *Nat. Mater.* **21**, 1050–1056 (2022).
16. Krauskopf, T., Mogwitz, B., Rosenbach, C., Zeier, W. G. & Janek, J. Diffusion limitation of lithium metal and Li–Mg alloy anodes on LLZO type solid electrolytes as a function of temperature and pressure. *Adv. Energy Mater.* **9**, 1902568 (2019).
17. Chen, Y. et al. Li metal deposition and stripping in a solid-state battery via Coble creep. *Nature* **578**, 251–255 (2020).
18. Wang, Z. et al. Creep-enabled 3D solid-state lithium-metal battery. *Chem* **6**, 2878–2892 (2020).
19. Wu, B. et al. The role of the solid electrolyte interphase layer in preventing Li dendrite growth in solid-state batteries. *Energy Environ. Sci.* **11**, 1803 (2018).
20. Otoyama, M. et al. Visualization and control of chemically induced crack formation in all-solid-state lithium-metal batteries with sulfide electrolyte. *ACS Appl. Mater. Interfaces* **13**, 5000–5007 (2021).
21. Mo, F. et al. Inside or outside: origin of lithium dendrite formation of all solid-state electrolytes. *Adv. Energy Mater.* **9**, 1902123 (2019).
22. Liu, X. et al. Local electronic structure variation resulting in Li 'filament' formation within solid electrolytes. *Nat. Mater.* **20**, 1485–1490 (2021).
23. Zhang, L. et al. Lithium whisker growth and stress generation in an in situ atomic force microscope-environmental transmission electron microscope set-up. *Nat. Nanotechnol.* **15**, 94–98 (2020).
24. Kasemchainan, J. et al. Critical stripping current leads to dendrite formation on plating in lithium anode solid electrolyte cells. *Nat. Mater.* **18**, 1105–1111 (2019).
25. Wang, M. J., Choudhury, R. & Sakamoto, J. Characterizing the Li-solid-electrolyte interface dynamics as a function of stack pressure and current density. *Joule* **3**, 2165–2178 (2019).
26. Schwietert, T. K. et al. Clarifying the relationship between redox activity and electrochemical stability in solid electrolytes. *Nat. Mater.* **19**, 428–435 (2020).
27. Wang, M., Wolfenstine, J. B. & Sakamoto, J. Temperature dependent flux balance of the $Li/Li_7La_3Zr_2O_{12}$ interface. *Electrochim. Acta* **296**, 842–847 (2019).
28. Wan, H. et al. F and N rich solid electrolyte for stable all-solid-state battery. *Adv. Funct. Mater.* **32**, 2110876 (2022).
29. Ning, Z. et al. Visualizing plating-induced cracking in lithium-anode solid-electrolyte cells. *Nat. Mater.* **20**, 1121–1129 (2021).
30. Jin, S. et al. Solid-solution-based metal alloy phase for highly reversible lithium metal anode. *J. Am. Chem. Soc.* **142**, 8818–8826 (2020).
31. Yang, C. et al. An electron/ion dual-conductive alloy framework for high-rate and high-capacity solid-state lithium-metal batteries. *Adv. Mater.* **31**, e1804815 (2019).
32. Hohenberg, P. & Kohn, W. Inhomogeneous electron gas. *Phys. Rev.* **136**, B864 (1964).
33. Kohn, W. & Sham, L. J. Self-consistent equations including exchange and correlation effects. *Phys. Rev.* **140**, A1133 (1965).
34. Kresse, G. & Hafner, J. Ab initio molecular dynamics for liquid metals. *Phys. Rev. B* **47**, 558 (1993).
35. Blöchl, P. E. Projector augmented-wave method. *Phys. Rev. B* **50**, 17953 (1994).
36. Kresse, G. & Furthmüller, J. Efficient iterative schemes for ab initio total-energy calculations using a plane-wave basis set. *Phys. Rev. B* **54**, 11169 (1996).
37. Perdew, J. P., Burke, K. & Ernzerhof, M. Generalized gradient approximation made simple. *Phys. Rev. Lett.* **77**, 3865 (1996).
38. Momma, K. & Izumi, F. VESTA 3 for three-dimensional visualization of crystal, volumetric and morphology data. *J. Appl. Crystallogr.* **44**, 1272–1276 (2011).

Acknowledgements

This work was supported by the US Department of Energy under award number DEEE0008856 (received by C.W.) and the Advanced Research Projects Agency-Energy under award DE-AR0000781 (received by C.W). We thank T. Deng for providing $LiNiO_2$ cathode material.

Author contributions

H.W. and C.W. conceived the idea for this project. H.W. prepared the materials and performed the characterization and electrochemical measurements. Z.W. and B.Z. conducted the simulations. Z.W. assisted on contact angle test and materials preparation. S.L. assisted on three-electrode cell tests. X.H. and W.Z. assisted on battery testing.

Competing interests

The authors declare no competing interests.

Additional information

Supplementary information The online version contains supplementary material available at https://doi.org/10.1038/s41560-023-01231-w.

Correspondence and requests for materials should be addressed to Chunsheng Wang.

Peer review information *Nature Energy* thanks the anonymous reviewers for their contribution to the peer review of this work.